Search for dark photon and dark matter signatures around electron-positron colliders

Xin Chen[a,b], Zhen Hu[a,b], Yongcheng Wu[c], Kai Yi[d]

[a]Department of Physics, Tsinghua University, Beijing 100084, China
[b]Center for High Energy Physics, Tsinghua University, Beijing 100084, China
[c]Ottawa-Carleton Institute for Physics, Carleton University, Ottawa, Ontario K1S 5B6, Canada
[d]School of Physics and Technology, Nanjing Normal University, 1 Wenyuan Road, 210046, China

Abstract

The search for a dark photon produced at e^+e^- colliders which subsequently decays into inelastic dark matter particles, is discussed. The heavier dark matter decays into a pair of visible charged particles and a lighter dark matter particle after traveling some distance. The visible decay products can be recorded by a dark matter detector made of emulsions and gas detectors, placed near the main e^+e^- detector. This setup can not only explore new parameter regions not reached before, but also re-open some regions thought to be excluded by previous experimental data. The physics potential for such a detector around BESIII and Belle II is presented.

Keywords: Dark photon, Inelastic dark matter, Long-lived particle

1. Introduction

The dark matter (DM) is well motivated by astrophysical observations, and it is believed to interact weakly with the Standard Model (SM) particles through some mediators like the dark photon. A number of fixed-target experiments, as well as collider-based ones, have searched for a dark photon, where it is produced from charged particles with a tiny coupling strength. The dark photon can decay back into charged SM particles, after flying some distance due to the small coupling and hence small decay width, which is the model of many fixed-target experiments (see [1] and references therein). When the dark photon mass is large and the coupling is not so small, it can decay promptly into a pair of charged SM particles or neutral DM ones, which has been studied at the electron-positron colliders such as BaBar [2, 3].

With ever more stringent limits obtained from direct DM detection experiments [4], a WIMP-like DM particle with mass $\gtrsim 10$ GeV is being severely constrained, and a lot of attention is being paid to light DM searches [5–8]. On the other hand, Cosmic Microwave Background (CMB) anisotropy result [9] excluded a DM particle mass $\lesssim 10$ GeV for the WIMP s-wave annihilation scenario consistent with the relic DM abundance. The tension can be relaxed with an inelastic DM model [10]. One of the two DM particles is in a heavy mass eigenstate, so it can further decay into a ground state DM and a charged SM particle pair. By detecting the charged pair, the existence of a DM sector with a dark photon mediator can be inferred. We here propose a new experimental setup to search for a dark photon that promptly decays into such a pair of DM particles near the e^+e^- colliders. The DM detector can be placed in the forward or central region where the heavy "excited" DM particles are more abundantly produced, but are difficult to be detected by the main e^+e^- detector.

2. Theoretical framework

At low energy, we assume an effective toy model with a dark photon mediator A' and complex scalar ϕ as the DM particle. The relevant Lagrangian reads

$$\begin{aligned}\mathcal{L} =& \mathcal{L}_{SM} - \frac{1}{4}A'_{\mu\nu}A'^{\mu\nu} + \frac{1}{2}m^2_{A'}A'_\mu A'^\mu - \epsilon e Q_f A'_\mu \bar{f}\gamma^\mu f + \\ & \left(D_\mu\phi\right)^* D^\mu\phi - \mu^2\phi^*\phi - \frac{1}{2}\rho^2\left(\phi\phi + \phi^*\phi^*\right), \end{aligned} \tag{1}$$

where A' is the dark photon, f is the SM fermion with charge Q_f, ϵ is the mixing parameter between the $U(1)_Y$ and $U(1)_D$ gauge fields, $D_\mu = \partial_\mu + ig_D A'_\mu$ is the covariant derivative with dark coupling parameter g_D, $\phi = (\phi_1 + i\phi_2)/\sqrt{2}$ is the complex scalar DM. The last term in Eq. 1 is a "Majorana"-like mass term that violates the $U(1)_D$ symmetry. Substituting $\phi_{1,2}$ for ϕ, we have

$$\begin{aligned}\mathcal{L} \supset & \frac{1}{2}\partial_\mu\phi_1\partial^\mu\phi_1 + \frac{1}{2}\partial_\mu\phi_2\partial^\mu\phi_2 - \frac{1}{2}\left(\mu^2+\rho^2\right)\phi_1^2 \\ & - \frac{1}{2}\left(\mu^2-\rho^2\right)\phi_2^2 - g_D A'_\mu\left(\phi_2\partial^\mu\phi_1 - \phi_1\partial^\mu\phi_2\right) \\ & + \frac{1}{2}g_D^2 A'_\mu A'^\mu\left(\phi_1^2+\phi_2^2\right). \end{aligned} \tag{2}$$

It is evident that the presence of the small ρ-term in Eq. 1 causes a mass splitting between the two real scalars ϕ_1 and ϕ_2, with mass $m_1 = \sqrt{\mu^2+\rho^2}$ and $m_2 = \sqrt{\mu^2-\rho^2}$, respectively. It is also possible to achieve a similar mass splitting for a fermionic DM by the presence of Majorana mass terms [11], but the scalar model we are studying will be general enough to cover similar kinematics.

Email addresses: xin.chen@cern.ch (Xin Chen), Zhen.Hu@cern.ch (Zhen Hu), ycwu@physics.carleton.ca (Yongcheng Wu)

3. DM relic density

The inelastic DM model we investigate here has several features to relax the tension between a light DM mass and the CMB constraint. The mass relation $m_{A'} > m_1 + m_2$ ensures that $\phi_2\phi_2 \to A'A' \to$ SM is closed, and the dominant coannihilation channel $\phi_1\phi_2 \to A'^* \to$ SM will be no longer active in the recombination era due to the depletion of ϕ_1, which therefore does not affect CMB much. The Lagrangian form in Eq. 2 means that the elastic scattering between ϕ_2 and SM particles are loop suppressed, and thus can evade the direct DM detection via nuclear recoil (apart from the fact that ϕ_2 is light). This type of dark photon decaying into inelastic light DM particles can be searched in e^+e^- collider experiments [11], such as Belle II or BESIII, with distinct signatures such as a mono-photon alone [3], or a mono-photon plus a pair of e^+e^- with a displaced vertex [12]. The inelastic DM has also been discussed in the context of hadron colliders covering a dark photon mass $\gtrsim$10 GeV [13], and fixed-target experiments suitable for a DM mass $\lesssim$1 GeV [14].

It is assumed that the dark and SM matter were in thermal equilibrium in the early universe. When the DM annihilation rate into SM particles falls below the Hubble expansion rate, the DM number density freezes out to the current relic density of $\Omega h^2 = 0.12$ [9]. The DM coannihilation rate for $\phi_1\phi_2 \to A'^* \to f\bar{f}$ is [11]

$$\sigma\upsilon = \frac{8\pi\epsilon^2\alpha\alpha_D m_1 m_2 \upsilon^2}{3\left[(m_1+m_2)^2 - m_{A'}^2\right]^2}, \tag{3}$$

where $\alpha = e^2/4\pi$, $\alpha_D = g_D^2/4\pi$, and υ is the relative velocity between ϕ_1 and ϕ_2. Contrary to the case of fermionic DM particles, this process is p-wave suppressed. Therefore, the scalar DM model provides an extra handle to relax the tension between a light DM and the CMB result in which a s-wave DM coannihilation is assumed [9]. As illustrated in [11, 12], the existing experimental limits favor a small mass splitting between ϕ_1 and ϕ_2, and to avoid DM overabundance, the masses of $\phi_{1,2}$ close to the threshold, $m_{A'} \simeq m_1 + m_2$, are preferred. This has two consequences: ϕ_1 produced at colliders tends to have a longer lifetime, and its flight direction is very much collinear with its mother dark photon. Because an on-shell dark photon is mainly produced in the forward detector direction (see Sec. 4), we propose putting a DM detector in the forward region to detect the decay products of ϕ_1, while for an off-shell dark photon, we propose putting it in the central region. To check the relic density compatibility, we employ `micrOMEGAs` [15] to perform numerical calculations of the density evolution.

4. Dark photon production at e^+e^- colliders

The main production diagrams of a dark photon together with an Initial State Radiation (ISR) photon, i.e., $e^+e^- \to \gamma A'$, at a e^+e^- collider are shown in Fig. 1.

The Born level differential cross section of the process $e^+e^- \to A'\gamma$ with respect to $\cos\theta$, where θ is the polar angle between the outgoing A' and the electron beam axis, can be expressed as [16]

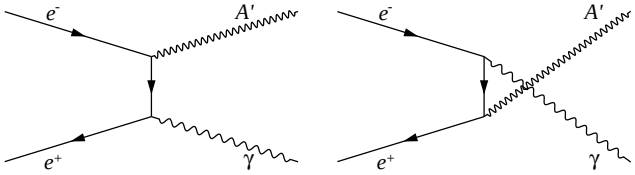

Figure 1: The production diagrams of an on-shell dark photon A' at a e^+e^- collider.

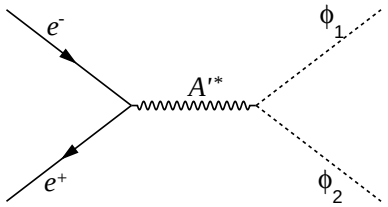

Figure 2: The production diagrams of an off-shell dark photon A' at a e^+e^- collider.

$$\frac{d\sigma}{d\cos\theta} = 2\pi\epsilon^2\alpha^2 \frac{\left(s+m_{A'}^2\right)^2 + \left(s-m_{A'}^2\right)^2\cos^2\theta}{s\left(s-m_{A'}^2\right)\left(s\sin^2\theta + 4m_e^2\right)}, \tag{4}$$

where s is the center of mass (CM) energy squared of the e^+e^- system, and m_e the electron mass. According to this expression, it can be seen that the dark photon is primarily produced in the very forward directions of a e^+e^- detector system. The production cross section increases with dark photon mass for a given $\sqrt{s}$, while for a given dark photon mass, it decreases with $\sqrt{s}$.

Apart from the on-shell A' production with an ISR photon, the DM particles can be directly produced through an off-shell A', as shown in Fig. 2. The differential cross section reads

$$\frac{d\sigma}{d\cos\theta} = \frac{\epsilon^2\alpha g_D^2 s}{32\left(s-m_{A'}^2\right)^2}\left(1-\frac{(m_1+m_2)^2}{s}\right)^{\frac{3}{2}} \cdot\left(1-\frac{(m_1-m_2)^2}{s}\right)^{\frac{3}{2}}\sin^2\theta. \tag{5}$$

The striking difference with respect to Eq. 4 is that ϕ_1 will be most abundantly produced in the central region of the detector.[1] If ϕ_1 is long-lived, no trace will be left inside the e^+e^- detector, whereas if it is short-lived, a pair of non-resonant soft tracks with a displaced vertex can be left inside, but they are very hard to be detected due to the collision background.

5. Dark photon decay

After A' is produced, it then promptly decays into a charged SM fermion pair, or dark scalars ϕ_1 and ϕ_2. The spin averaged

[1] In the case of fermionic DM, for $m_1 + m_2$ close to $\sqrt{s}$ favored by the relic density, the angular probability of ϕ_1 is more isotropic.

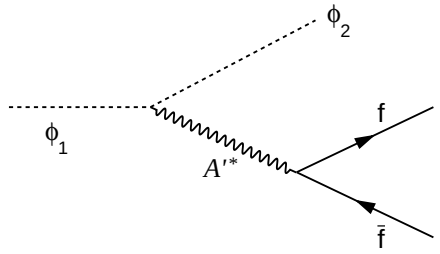

Figure 3: The decay diagram of a heavier dark scalar ϕ_1 into the lighter ϕ_2 and a $f\bar{f}$ pair through an off-shell A'^*.

A' decay width to each final state can be expressed as

$$\Gamma(A' \to f\bar{f}) = \frac{1}{3}\epsilon^2 Q_f^2 \alpha m_{A'} \left(1 + \frac{2m_f^2}{m_{A'}^2}\right)\left(1 - \frac{4m_f^2}{m_{A'}^2}\right)^{\frac{1}{2}}, \quad (6)$$

$$\Gamma(A' \to \phi_1\phi_2) = \frac{g_D^2}{48\pi} m_{A'} \left(1 - \frac{2(m_1^2 + m_2^2)}{m_{A'}^2} + \frac{m_1^4 + m_2^4 - 2m_1^2 m_2^2}{m_{A'}^4}\right) \cdot \left(1 - \frac{(m_1 + m_2)^2}{m_{A'}^2}\right)^{\frac{1}{2}} \left(1 - \frac{(m_1 - m_2)^2}{m_{A'}^2}\right)^{\frac{1}{2}}, \quad (7)$$

where m_f denotes the charged fermion mass ($f = e, \mu, u, d, s$). The partial decay width into quarks can be collectively named Γ_{had}, and can be effectively evaluated using the experimental R data [17], which is defined as

$$R(\sqrt{s}) = \frac{\sigma(e^+e^- \to \text{hadrons})}{\sigma(e^+e^- \to \mu^+\mu^-)}. \quad (8)$$

This experimental data input starts from $\sqrt{s} = 0.3$ GeV (just above the $\pi\pi$ mass threshold), with which Γ_{had} can be expressed as

$$\Gamma_{had} = \Gamma_{\mu\mu} \cdot R(\sqrt{s} = m_{A'}). \quad (9)$$

Since a small mass splitting is preferred by the relic density constraint, the signal mass range we consider would mostly mean a mass splitting below the ρ^0 meson threshold. This means that the hadronic contribution will be small, and the hadronic final state will be dominated by a $\pi^+\pi^-$ pair. When g_D is orders of magnitude larger than ϵ, A' will predominantly decay into the dark final state $\phi_1\phi_2$. Namely, the branching ratio (BR) of $A' \to \phi_1\phi_2$ will be large, which is the case we consider.

6. Heavier DM particle decay

The ϕ_1 will fly for some distance, and then decays into ϕ_2 and a $f\bar{f}$ pair through an off-shell A'^*, as shown in Fig. 3.

The partial decay width of the three-body decay $\phi_1 \to \phi_2 f\bar{f}$ can be expressed as

$$d\Gamma(\phi_1 \to \phi_2 f\bar{f}) = \frac{\epsilon^2 Q_f^2 \alpha g_D^2}{8\pi^2 m_1^3 (m_{f\bar{f}}^2 - m_{A'}^2)^2} \Big[(m_{\bar{f}\phi_2}^2 - m_f^2)(m_1^2 + m_2^2 + m_f^2 - m_{f\bar{f}}^2 - m_{\bar{f}\phi_2}^2) - m_1 m_2\Big] dm_{f\bar{f}}^2 dm_{\bar{f}\phi_2}^2, \quad (10)$$

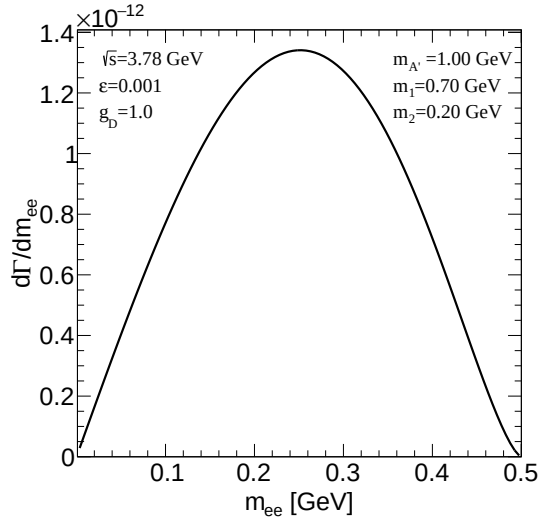

Figure 4: The differential decay width of $\phi_1 \to \phi_2 e^+e^-$ as a function of m_{ee}, with the chosen parameters indicated in the plot.

where $m_{f\bar{f}}$ denotes the $f\bar{f}$ pair invariant mass, and $m_{\bar{f}\phi_2}$ the invariant mass of $\bar{f}$ and ϕ_2. After integrating out $m_{\bar{f}\phi_2}$, the partial decay width becomes

$$\frac{d\Gamma_{\phi_1}}{dm_{f\bar{f}}} = \frac{\epsilon^2 Q_f^2 \alpha g_D^2}{24\pi^2 m_1^3 (m_{f\bar{f}}^2 - m_{A'}^2)^2 m_{f\bar{f}}^2} \Big[(m_1^2 - m_2^2 - m_{f\bar{f}}^2)^2 (m_{f\bar{f}}^2 + 2m_f^2) - 4m_2^2 m_{f\bar{f}}^4 - 8m_2^2 m_f^2 m_{f\bar{f}}^2\Big] \Big(m_{f\bar{f}}^2 - 4m_f^2\Big)^{\frac{1}{2}} \Big[(m_1^2 - m_2^2 - m_{f\bar{f}}^2)^2 - 4m_2^2 m_{f\bar{f}}^2\Big]^{\frac{1}{2}}, \quad (11)$$

and the allowed range for $m_{f\bar{f}}$ is $2m_f \le m_{f\bar{f}} \le (m_1 - m_2)$. When $f = e$, the differential decay width of ϕ_1 is shown in Fig. 4. It is evident that the ee pair mass has a broad spectrum spanning the whschemole allowed mass range. For the hadronic three-body decays of ϕ_1, as for the case of A', the R input is used.

Since it is produced from the A' decay, the flight length (d) of ϕ_1 is determined by its Lorentz boost factor γ_1 and its total decay width by

$$d = \frac{\gamma_1 \beta_1}{\sum_f \Gamma_{\phi_1 \to \phi_2 f\bar{f}}}, \quad (12)$$

where β_1 is the speed of ϕ_1. The ϕ_1 boost factor varies from event to event, but an average value can be obtained by averaging over the angle θ_1^* in Eq. 14 introduced in the next section. The d distributions as a function of m_1 and m_2 are shown in Fig. 5, in the setting of BESIII. It is evident that as the mass splitting $m_1 - m_2$ increases, the flight length d decreases, and the region with $d < 1$ m is best suitable for the displaced vertex search in [12]. On the other hand, as mentioned in Sec. 3, the DM relic density constraint favors a small mass splitting (hence a larger d), which is the focus in this work.

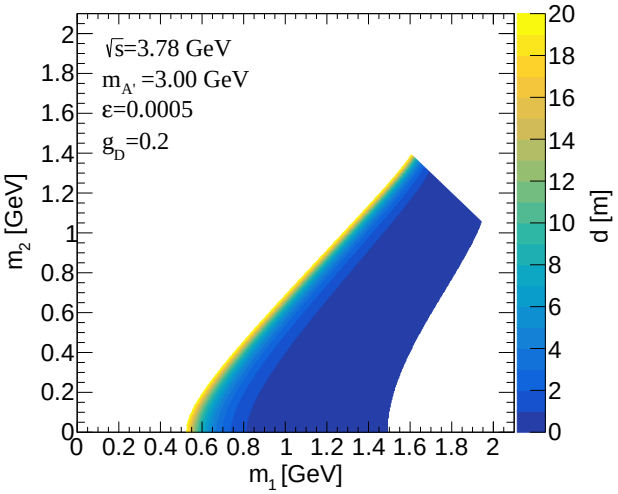

Figure 5: The distribution of ϕ_1 average flight length d as a function of m_1 vs. m_2, with the chosen parameter values indicated in the plot. The ϕ_1 Lorentz boost factor is based on Eq. 14 but averaged over θ_1^*.

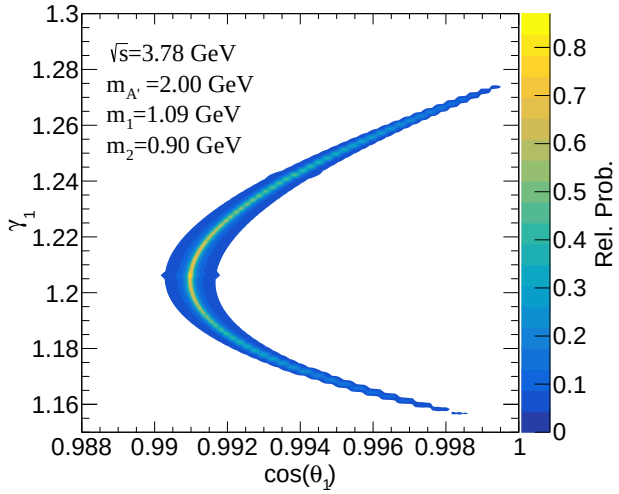

Figure 6: The 2-D probability distribution of $\cos\theta_1$ vs. Lorentz boost factor γ_1 of ϕ_1 in the e^+e^- lab frame, with the chosen parameters indicated in the plot. The color scale indicates relative probability.

7. Heavier DM particle distributions in the on-shell case

The angular distribution of ϕ_1 from an off-shell A' decay is already given in Eq. 5. For the case of on-shell A', the double differential cross section for the ϕ_1 production, in the narrow width approximation and with full spin correlation between $e^+e^- \to \gamma A'$ and $A' \to \phi_1\phi_2$, is proportional to

$$\begin{aligned}\frac{d\sigma}{d\Omega d\Omega_1^*} \propto & \frac{1}{s\left(s\sin^2\theta + 4m_e^2\right)}\left\{\left(s+m_{A'}^2\right)^2 + \left(s-m_{A'}^2\right)^2\cos^2\theta\right. \\ & -\left[\left(s-m_{A'}^2\right)^2 + \left(s+m_{A'}^2\right)^2\cos^2\theta\right]\cos^2\theta_1^* \\ & + 4m_{A'}\sqrt{s}\left(s+m_{A'}^2\right)\sin\theta_1^*\cos\theta_1^*\cos\phi_1^*\sin\theta\cos\theta \\ & \left.-4m_{A'}^2 s\sin^2\theta_1^*\cos^2\phi_1^*\sin^2\theta\right\}, \end{aligned} \tag{13}$$

where Ω (Ω_1^*) is the solid angle of A' (ϕ_1) in the e^+e^- lab (A' rest) frame, and θ_1^* and ϕ_1^*[2] are the polar and azimuth angles of Ω_1^*, with the flight direction of A' in the e^+e^- lab frame as the polar axis for Ω_1^*.

Contrary to Eq. 4 where A' is produced primarily in the forward ($\theta = 0$ or π) region, it is seen from Eq. 13 that when $\theta \to 0$ or π, and $\theta_1^* \to 0$, the cross section vanishes, which creates a "hole" in the very forward region. With Ω and Ω_1^* specified, the energy of ϕ_1 in the e^+e^- lab frame can be expressed as

$$\begin{aligned}E_1 = & \frac{s+m_{A'}^2}{4\sqrt{s}}\left(1+\frac{m_1^2-m_2^2}{m_{A'}^2}\right) + \\ & \frac{s-m_{A'}^2}{4\sqrt{s}}\left[\left(1+\frac{m_1^2-m_2^2}{m_{A'}^2}\right)^2 - \frac{4m_1^2}{m_{A'}^2}\right]^{\frac{1}{2}}\cos\theta_1^*, \end{aligned} \tag{14}$$

and the angle between its flight direction and the electron beam axis in the same frame (θ_1) can be determined via

$$\begin{aligned}\cos\theta_1 = & \left\{\left[s-m_{A'}^2+(s+m_{A'}^2)\beta_1^*\cos\theta_1^*\right]\cos\theta - \right. \\ & \left. 2\sqrt{s}m_{A'}\beta_1^*\sin\theta_1^*\cos\phi_1^*\sin\theta\right\}\cdot\left\{4sm_{A'}^2\beta_1^{*2}\sin^2\theta_1^* + \right. \\ & \left.\left[s-m_{A'}^2+(s+m_{A'}^2)\beta_1^*\cos\theta_1^*\right]^2\right\}^{-\frac{1}{2}}, \end{aligned} \tag{15}$$

where β_1^* is a constant defined as

$$\beta_1^* = \left(1-\frac{4m_{A'}^2m_1^2}{\left(m_{A'}^2+m_1^2-m_2^2\right)^2}\right)^{\frac{1}{2}}. \tag{16}$$

Based on Eq. 13-16, the 2-D probability density distribution of ϕ_1 Lorentz boost factor γ_1 and its $\cos(\theta_1)$ in the lab frame for a particular parameter set is shown in Fig. 6,[3] and the differential cross section of ϕ_1 as a function of $\cos(\theta_1)$ is shown in Fig. 7 in the vicinity of $\theta_1 = 0$.

8. Dark matter decay detector

To detect the visible decay products of ϕ_1, we propose to use an emulsion plus Micro-Pattern Gaseous Detector (MPGD) design. Emulsion detectors have been used in OPERA [18], DsTau [19] and FASERν [20] experiments. Our emulsion design has a multitude of thin layers, each of which consists of a 0.5 mm thick invariant alloy (consists of 63.8% iron, 36.0% nickel and 0.2% carbon) plate and 0.3 mm thick emulsion sheet. The invariant alloy has the advantage of a low thermal expansion coefficient, which makes the emulsion sheets alignment less susceptible to temperature variations. Each emulsion sheet

[2] Note that ϕ_1^* is also the angle between the plane formed by the beam axis and outgoing A', and the plane formed by the A' decay products.

[3] The irregular boundaries are numerical artifacts.

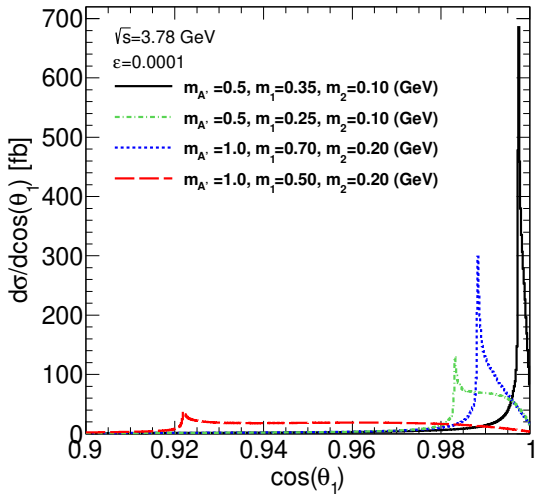

Figure 7: The differential cross sections of ϕ_1 as a function of $\cos\theta_1$ in the e^+e^- lab frame, corresponding to four different sets of chosen parameters indicated in the plot.

consists of a 200 μm thick base (made of, e.g., cellulose acetate), sandwiched between two emulsion films of 50 μm thickness, as illustrated in Fig. 8(a). The emulsion consists mainly of AgBr and gelatin material. The silver bromide crystals are sensitive to ionization by charged particles passing through the emulsion, and have a typical size of 0.2 μm. Therefore, the emulsion can have a position measurement of tracks with a precision below 1 μm, which makes it ideal for our purpose of detecting a pair of charged particles (ee, $\mu\mu$ or $\pi\pi$) with a common vertex.

The AgBr crystal has a band gap of about 2.5 eV. Photons radiated from charged particles incident on the AgBr crystal grain produce electrons which interact to yield silver atoms. More photons will induce a larger concentration of silver atoms, containing from 4 to tens of silver atoms, which form an invisible latent image. During film development, the latent image is amplified chemically by an order of $\sim 10^8$ and silver filaments are formed. After image fixing (removing the remaining silver salts), these silver filaments can be read out under microscopes. At the reconstruction level, sequences of aligned grains will be recognized and form tracks of charged particles. With the Geant4 [21] simulation it is found that, on average, a 10 MeV electron or positron travels through about 5 emulsion sheets, which amounts to 10 mini-track measurements (each emulsion sheet has two films on each side). This can be a threshold cut on the tracks in this work.

To distinguish backgrounds from cosmic muons and the associated secondary particles (mostly photons, and a small amount of hadrons) produced by the interaction between the muons and upstream material, thin MPGD layers are sandwiched between blocks of emulsion layers. A suitable design of MPGD that meet our requirement of thin thickness ($\lesssim$1 cm), good spatial ($\sim$50 mum) and time resolution (a few ns) can be the Micro-Resistive WELL (μRWELL) detector [22]. Track segments in the MPGD layers can be matched with those in the emulsion blocks to provide timing information. If the time of a MPGD segment coincides with that of a cosmic muon or a beam background photon, the matched track in the emulsion is not considered. The time of cosmic muons can be obtained through scintillator fibers encasing the whole active detector and the lead shield, as illustrated in Fig. 8(b). The time resolution of a scintillator is usually at $\sim$1 ns level. Each emulsion block (yellow) contains 40 emulsion layers and thus is 3.2 cm thick, while each MPGD layer (cyan) is 0.8 cm thick. There is a 10 cm thick lead shield between the detector and outside scintillator covering. This shield can prevent inner signal track from reaching the scintillator, and can also help blocking photons from outside sources (beam background) entering the detector, if it is put in a place close to the beam. There can be 33 emulsion blocks and MPGD layers, making the active part of the detector 1.32 m long. The cross sectional area of the emulsion and MPGD can be 20 cm×30 cm.

We propose to place the detector near a e^+e^- collider such as BESIII and Belle II. One possible placement around BESIII is illustrated in Fig. 9(a) in the forward direction. The DM detector is facing toward the interaction point (IP). For BESIII (Belle II), the distance between the IP and its front area could be 6 m (7 m), and the perpendicular distance between the front area center and the beam axis could be 0.84 m (1 m).[4] For the case of an off-shell A' and scalar DM, another placement is illustrated in Fig. 9(b), where the detector is placed 4 m away from the IP in the central region facing the barrel. The probability distributions of polar vs. azimuthal angle of particle ϕ_1 in the e^+e^- lab frame in the forward direction are shown in Fig. 10, where the areas covered by the proposed detector are indicated by white rectangular boxes. The signal acceptance efficiencies of the detector for some different parameters and detector positions are given in Table 1. Depending on specific model parameters, acceptances in the two forward detectors can be very different. This enables us to treat one as the signal detector, and the other as the background control detector. Note that the same purpose can be fulfilled by putting both forward detectors the same perpendicular distance off from the beam, but at different lengths away from the IP. Although the central detector's acceptance is much smaller than in the forward case (Table 1), it can cover a signature that is very difficult to be detected by the main e^+e^- detector.

The tracks from ϕ_1 decay inside the detector are simulated by Geant4 [21] with the Physics List `FTFP_BERT`, and a few examples can be found in Fig. 11(a-c) (MPGD not included). The signal is characterized by two tracks sharing a common vertex inside the detector, which is highly distinguishable from background particles (mainly muons) with single tracks going through the whole detector, as illustrated by Fig. 11(d). For low energy muons and charged pions, they lose energy mainly via ionization, while electrons of similar energy level lose energy substantially via bremsstrahlung. This explains the shorter trajectory lengths of electrons in Fig. 11. Muons and pions can

[4] There is a small beam crossing angle at the beam interaction region, and Belle II beams are asymmetric in energy. These effects can be simulated, but are not taken into account in this work for simplicity.

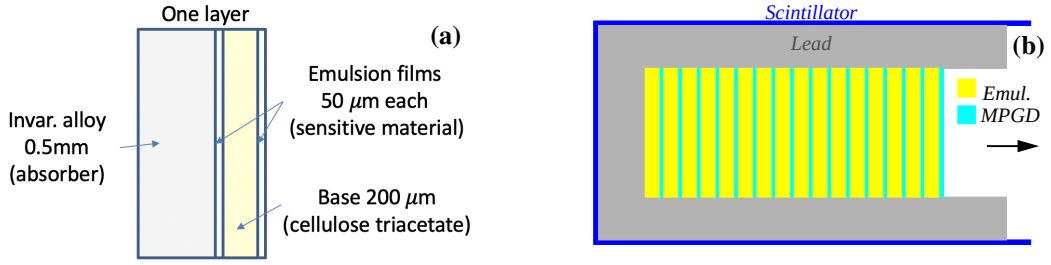

Figure 8: The illustration of an emulsion layer (a) and the cross sectional sketch of the proposed detector (b).

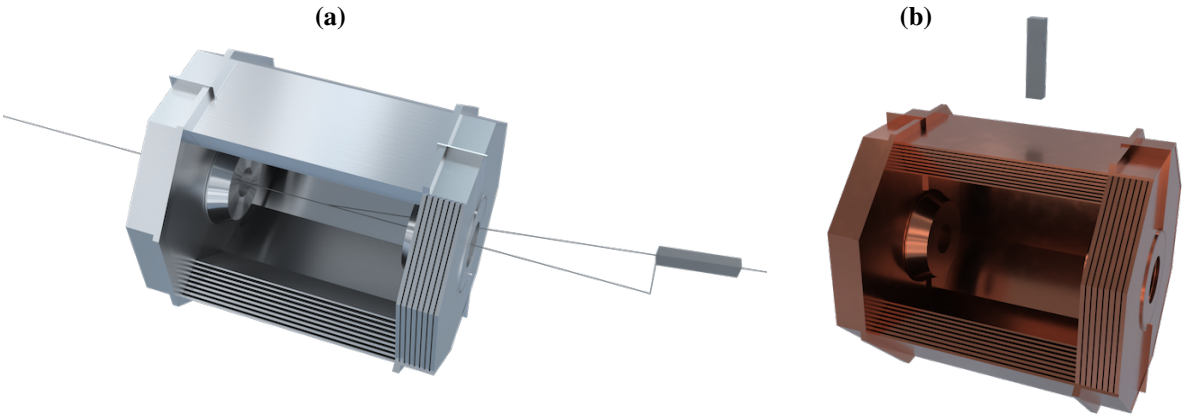

Figure 9: (a) The schematic view of the DM detector's position (6 m away from the IP, and 0.84 m off from the beam axis) relative to the BESIII detector (only the muon identifier is shown). (b) The position of a DM detector placed in the central region (4 m away from the IP) relative to the BESIII or Belle II detector.

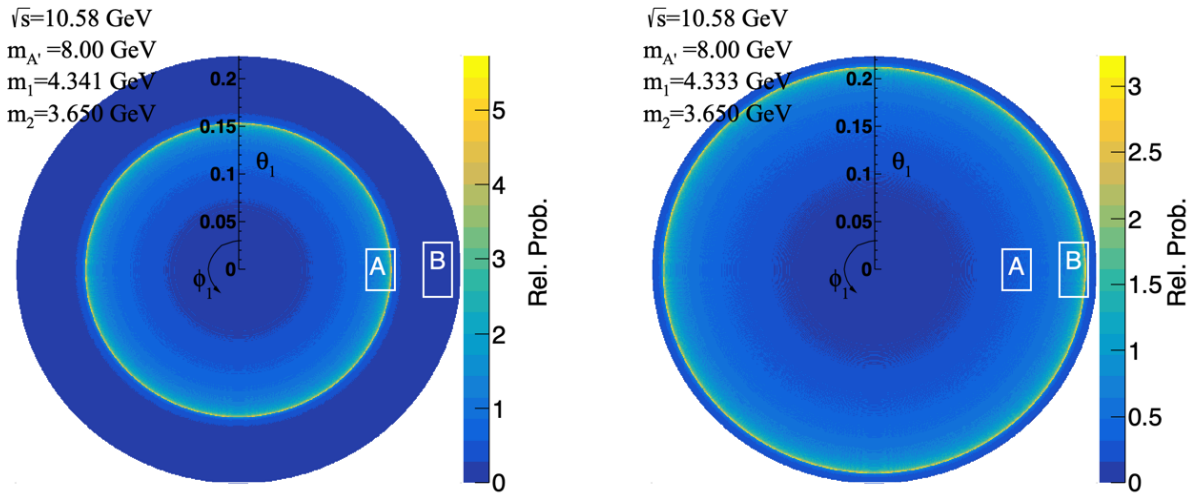

Figure 10: The probability distribution of polar vs. azimuthal angle of particle ϕ_1 in the e^+e^- lab frame, with the chosen parameters for an on-shell A' indicated in the plot. The cross sectional areas of two DM detectors are indicated by the white box A (0.2×0.3 m^2) and B (0.2×0.4 m^2). Detector A (B) is placed 1 m (1.4 m) off the beam axis. Both are 7 m away from the IP. The color scale indicates relative probability.

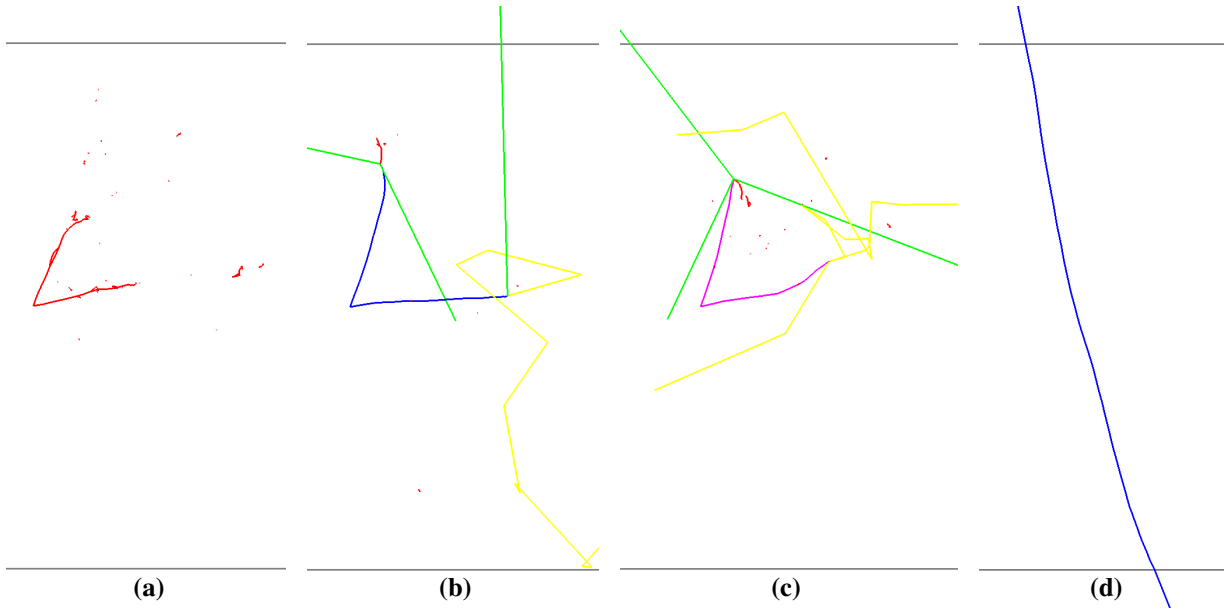

Figure 11: The tracks of a e^+e^- (a), $\mu^+\mu^-$ (b), $\pi^+\pi^-$ (c) pair coming from a ϕ_1 decay, and a cosmic muon (d) in the DM detector simulated with Geant4 (MPGD not included). The cosmic muon has an energy of 1 GeV, and all other tracks have a kinetic energy of 100 MeV. The yellow (green) trajectories represent neutrons (neutrinos), which leave little or no energy in the detector. The cross sectional view along the z-axis is shown and the horizontal gray lines indicate the top and bottom boundaries of the detector.

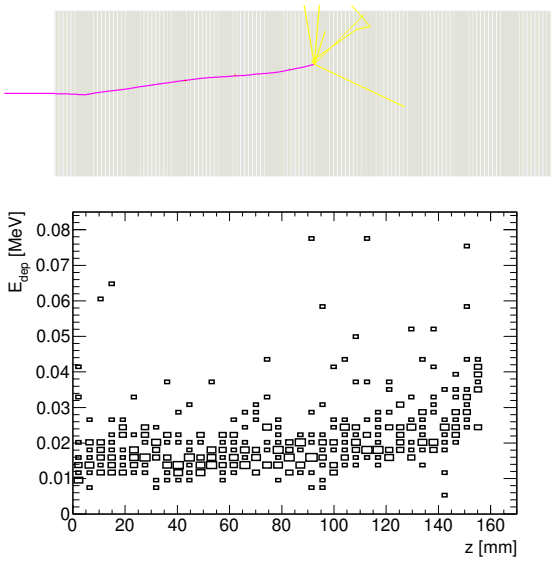

Figure 12: The trajectory (in purple) of a 200 MeV (kinetic energy) charged pion entering the detector along the z direction from outside (top), and its energy deposited in each emulsion film (bottom), based on the Geant4 simulation.

Table 1: For the on-shell A', the efficiencies of signal acceptance by the two DM detectors with two different mass parameter settings , with $\sqrt{s}$ = 10.58 GeV and the detectors in the forward position as illustrated in Fig. 10. For the off-shel l A', the same efficiency with the DM detector placed in the central barrel position, as illustrated in Fig. 9(b).

On-shell case (GeV)	ϵ_A	ϵ_B
$m_{A'} = 8.0, m_1 = 4.341, m_2 = 3.650$	0.976%	0.065%
$m_{A'} = 8.0, m_1 = 4.333, m_2 = 3.650$	0.194%	0.816%
Off-shell case (GeV)	ϵ_{off}	
$m_{A'} = 14.0, m_1 = 5.00, m_2 = 4.85$	0.045%	

Table 2: The estimated number of muons per cm^2 from BESIII (at $\sqrt{s}$ = 3.78 GeV) or cosmic sources onto the DM detector for a given integrated luminosity or period. The production cross section at the $\psi(3686)$ resonance is taken from [23]. The rate for cosmic muons is based on sea level with no shielding.

	non-resonant	$\psi(3686)$	cosmic
lumi. or period	10 fb^{-1}	4.5 fb^{-1}	6 months
muons/cm^2	20.2	74.4	0.28×10^6

decay into electrons and neutrinos, or interact with the nuclei to release neutrons, at the end of the trajectory. Both neutrons and neutrinos leave little or no energy in the detector.

It is also possible to obtain timing information from the pattern of energy deposition in the emulsion films alone. Figure 12 shows the path of a 200 MeV pion entering the detector along the z direction, and the energy deposited per emulsion film. It can be seen that at the end of the track when the pion slows down, more energy loss due to ionization is deposited. This trend helps to tell the pion's direction of travel in the detector.

9. Background events

With electrons, photons and hadrons absorbed by upstream detector and beam pipe related infrastructures, the main background particles entering the DM detector are muons. They consist of cosmic muons and muons produced in e^+e^- collisions, which are described in the following subsections. A summary of the contributions from different background sources is given in Table 2.

9.1. Collider muons

Non-resonant $\mu^+\mu^-$ events are constantly produced in the e^+e^- collisions, whose differential cross section is expressed as

$$\frac{d\sigma}{d\cos\theta} = \frac{\pi\alpha^2}{2s}\left(1+\cos^2\theta\right). \quad (17)$$

On the other hand, $\mu^+\mu^-$ events can be also produced from hadron resonances such as J/ψ and $\psi(2S)$. Because they are vectors, their differential cross sections have the same angular dependence as in Eq. 17. These collider muons have very small efficiency of acceptance in the DM detector, and contribute far less background events than the cosmic source, as shown in Table 2.

9.2. Cosmic muons

If the proposed DM detector is built above ground (BESIII) or near ground (Belle II), comic-ray muons could be a main background. At sea level, assuming a flat Earth, the muon flux Φ can be approximately defined as

$$\Phi(\theta) = I_0\cos^{n-1}\theta, \quad (18)$$

where the zenith angle θ is the angle between the muon's momentum and the normal of the Earth's surface, and I_0 is the vertical ($\theta = 0$) muon flux integrated over energy. With parameters $n \approx 3$ and $I_0 \approx 85.6\pm2.4\ \mathrm{m^{-2}s^{-1}sr^{-1}}$, obtained by fitting the previous cosmic-ray muon measurements, the muon flux roughly follows a $\cos^2\theta$ distribution [24, 25]. The integrated muon flux can be obtained as

$$\Phi = \int_{\theta=0}^{\pi/2}\int_{\phi=-\pi}^{\pi} I_0\cos^2\theta d\cos\theta d\phi = 179.3\ \mathrm{Hz/m^2}. \quad (19)$$

To control the track occupancy under $10^6/\mathrm{cm}^2$ [26] for the post-processing, the emulsion films have to be replaced before this limit is reached. With the estimated rate in Eq. 19, after 6 months' data taking, the cosmic occupancy will reach $0.28\times10^6/\mathrm{cm}^2$. Therefore, replacement of the emulsion films in every 6 months is good enough. The Belle II detector is placed 11 meters underground in a pit. The underground rock can help shield the cosmic muons, making this background less serious than for BESIII. Bremsstrahlung photons from muons will give rise to EM showers containing collimated and soft e^+e^- pairs, whose topology can be well distinguished from the signal. An emulsion detector track reconstruction algorithm is needed to perform a detailed study. On the other hand, the MPGD+scintillator design can also significantly reject such kind of tracks, whose time coincides with the cosmic muons hitting the outside scintillator.

9.3. K_L^0 and beam backgrounds

We simulated the Belle II production of K_L^0 with `EvtGen` [27] for K_L^0's from B meson decay, and with `KKMC` [28, 29] from continuum ($u/d/s/c$) and $\tau^+\tau^-$ decay. The total cross section for $\Upsilon(4S)$ (continuum and $\tau\tau$) is 1.110 nb [30] (4.512 nb). About 69.4% (26.0%) events in the inclusive $\Upsilon(4S)$ (continuum and $\tau\tau$) sample contain a K_L^0. The K_L^0 energy spectrum entering the DM detector is shown in Fig. 13, from which one can see that K_L^0 from B decay is much softer than from the continuum.

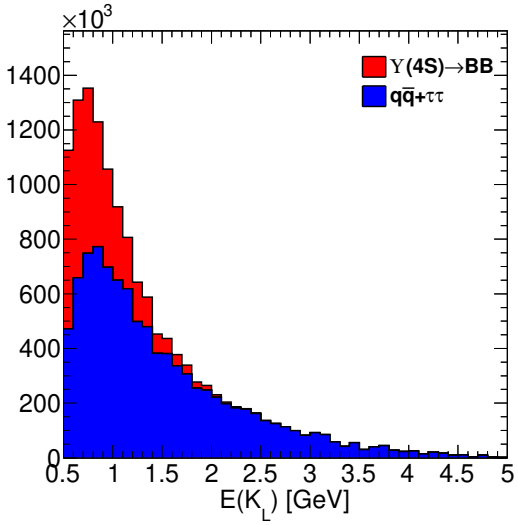

Figure 13: The K_L^0 energy spectrum entering the proposed DM detector at Belle II, estimated with 50 $\mathrm{ab^{-1}}$.

To block these K_L^0's from IP, we propose putting a 1.3 m long of tungsten slab in front of the forward DM detector, fully covering the detector cross section. We then simulated the passage of K_L^0 through the tungsten shield with Geant4, assuming the DM detector is 7 m away from the IP. We further assume a 30 cm of shielding material (iron) at about 2 m from the IP due to the beam focusing magnet iron, the cryostat and the magnetic return yoke iron.[5] In summary, with this simulation setup and the energy spectrum in Fig. 13, we found that the probability for a K_L^0 to arrive at the DM detector is 4×10^{-8}. As a result, we expect ~0.5 K_L^0 in the DM detector coming from the IP with 50 $\mathrm{ab^{-1}}$ of data. For the central DM detector, since the magnetic flux return yoke is thick and can already provide a large amount of shielding for K_L^0, a shorter tungsten shielding will be sufficient.

We also simulated cosmic muons (consists of 45% μ^- and 55% μ^+) passing through 11 m of rock (whose density is ~2.5 $\mathrm{g/cm^3}$) for the Belle II environment, and found that there are ~12 K_L^0's from cosmic muons' photonuclear interaction with the upstream rock material passing through the DM detector per year. Most of them will interact hadronically within the DM detector volume, instead of decay ($\lesssim$1 %). Therefore, the double detector setup described in Sec. 8 becomes efficient to control these background events. In addition, tracks induced by this kind of K_L^0's, as well as other neutral hadrons, can be tagged by the MPGD+scintillator design, since they happen at the same time when the cosmic muons pass through the detector.

Beam backgrounds, which include the Touschek effect, beam-gas scattering, synchrotron radiation and radiative Bhabha processes, can also affect the detector. The Touschek effect and beam-gas scattering will cause beam particles deviate

[5] Exact details to be confirmed with the experiment.

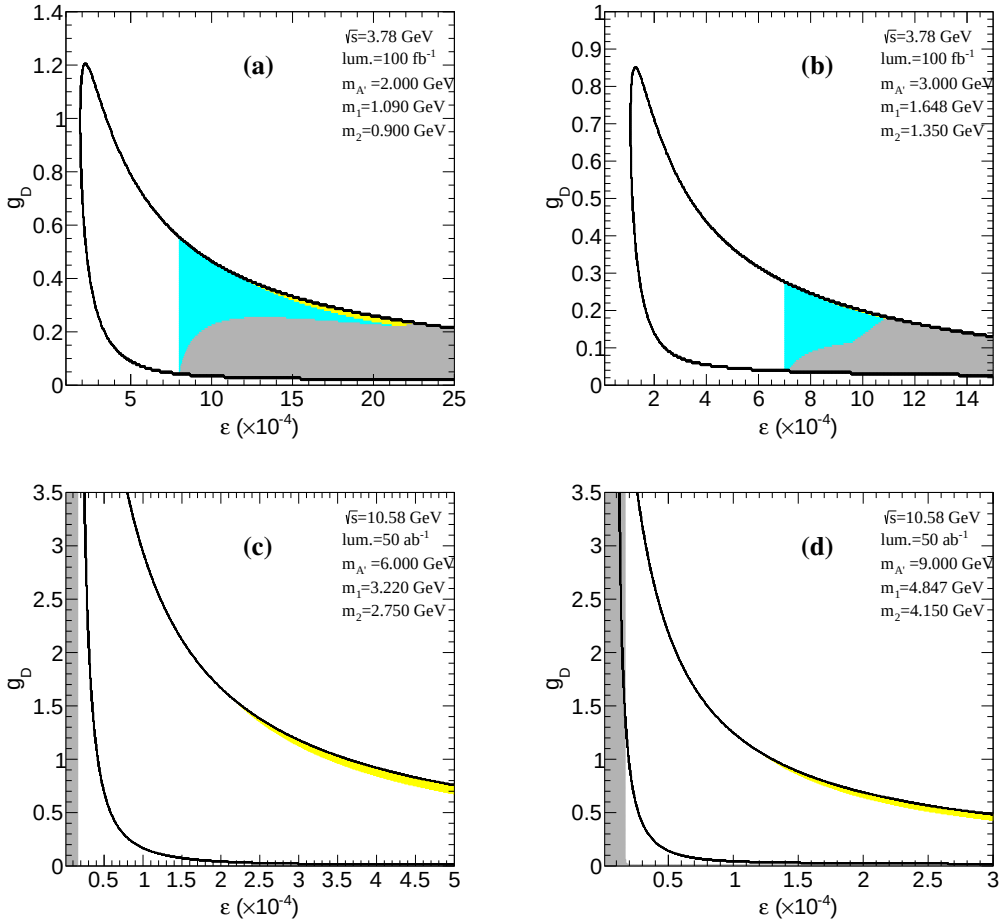

Figure 14: The 90% CL exclusion regions assuming zero background in ϵ vs. g_D with two forward DM detectors placed on each side of BESIII (a, b) and Belle II (c, d), for the chosen model parameters (A' is on-shell) indicated in the plots. The gray areas in (a, b) have been excluded by BaBar, and those in (c, d) are excluded by the relic density constraint. The cyan region could have otherwise been excluded by [3], but re-opens for exploration in the new model. The yellow area has an average ϕ_1 flight length $d < 1$ m, which is the best suitable region for the displaced vertex plus photon search proposed in [12].

from their nominal energy and hit the beam pipe walls or collimators. Majority of the gammas from the developed EM showers are soft and can be well shielded by the lead in Fig. 8(b). For example, a 10 cm thick lead can block most photons with energy below a few GeV. Again, the MPGD+scintillator design works against these backgrounds as well. The synchrotron radiation is at tens of keV level, and hence not a big background source. The gamma from radiative Bhabha process can hit the magnet iron and produce a lot of neutrons. These neutrons can be well shielded by the same tungsten slab used to shield K_L^0's. However, a detailed simulation of these effects needs a good knowledge from the detector and accelerator, which is out of the scope of this work. Finally, we point out an interesting scenario where multiple new long-lived particles exist, and an additional secondary production of these particles may take place in the shielding material right in front of the detector, as described in [31]. Our detector setup is also sensitive to this scenario.

10. Signal sensitivity

The expected number of signal events in the DM detector for an on-shell dark photon can be calculated as:

$$N_{sig} = \mathcal{L}\sigma(e^+e^- \to \gamma A')\mathrm{BR}(A' \to \phi_1\phi_2)\epsilon_A \left(e^{-\frac{a}{d}} - e^{-\frac{a+L}{d}}\right), \tag{20}$$

where $\mathcal{L}$ is the integrated luminosity of data, $L = 1.32$ m, d is calculated as in Eq. 12, and $a = 6$ m (7 m) for BESIII (Belle II). For an off-shell A', it is calculated instead by

$$N_{sig} = \mathcal{L}\sigma(e^+e^- \to A'^* \to \phi_1\phi_2)\epsilon_{off} \left(e^{-\frac{a}{d}} - e^{-\frac{a+L}{d}}\right), \tag{21}$$

where $a = 4$ m for Belle II.

In the case of an on-shell A', the parameter spaces in ϵ vs. g_D for some specific choices of model parameters with 90% CL exclusion for BESIII (Belle II) are shown in Fig. 14, based on 100 fb^{-1} (50 ab^{-1}) of data, when zero background and 100% signal reconstruction efficiency are assumed. The gray area has been excluded by BaBar $A' \to ll$ ($l = e, \mu$) [2], or $A' \to$ invisible search [3]. When ϵ is large and g_D is small, BR($A' \to ll$) might be too large and would have been excluded by [2]. This is the case when

$$\epsilon > \frac{\epsilon_1}{\sqrt{\mathrm{BR}(A' \to ll)}}, \tag{22}$$

where ϵ_1 is the limit on ϵ taken from [2]. On the other hand, the search for an invisible A' is based on mono-photon events at BaBar. If ϕ_1 decays inside the BaBar detector with visible energy depositions, this event will not be categorized into mono-photon any more. Considering the BaBar detector size, we roughly require that ϕ_1 has to fly by at least 2 m away from IP for the event to be a mono-photon candidate. This means that events satisfying the following condition would have been excluded by BaBar $A' \to$ invisible search:

$$\epsilon > \epsilon_2 e^{1/d}, \tag{23}$$

where ϵ_2 is the limit on ϵ taken from [3]. The combination of Eq. 22-23 are excluded in gray in Fig. 14(a, b) and 15. Figure 14-15 assume two identical DM detectors are placed on each side of the main e^+e^- detector. The cyan regions in Fig. 14 could have otherwise been excluded by [3], but are allowed according to Eq. 23. The yellow regions have a ϕ_1 with $d < 1$ m, which is the best suitable region for the displaced search proposed in [12]. Compared to BESIII, Belle II can probe higher dark photon masses, and sensitive to ϵ values lower by an order of magnitude. For $m_{A'} > 8$ GeV where the mono-photon search is difficult due to the radiative Bhabha background, the propose DM detector can well cover this parameter region.

Similar plots showing the relations between ϵ and m_2, or ϵ and $\Delta m/m_2$, are in Fig. 15 for Belle II with 50-500 fb^{-1} of data. The parameters regions with $m_2 > 1$ GeV that are hard to be covered by fixed target experiments, can be well reached. In all these plots, an optimal detector acceptance of 0.9% is assumed. For the detector placed at box A in Fig. 10, this means that a relation of $1 - (m_1 + m_2)/m_{A'} = (0.228 - 0.0223 m_{A'}) \cdot \exp(-0.489 m_{A'})$ (for $m_{A'} \leq 10$ GeV) should be satisfied. This relation is obtained by a fit to different $m_{A'}$ and $m_{1,2}$ values where an optimal acceptance is achieved. As mentioned in Sec. 3, these parameter settings, in which $m_1 + m_2$ is very close to $m_{A'}$, are also favored by the DM relic density constraint.

In the case of an off-shell A', the parameter spaces in ϵ vs. g_D for some specific choices of model parameters with 90% CL exclusion for Belle II are shown in Fig. 16, when zero background and 100% signal reconstruction efficiency are assumed again. In this figure, light (dark) gray areas are excluded by the relic density constraint (LEP model-independent search [32]).

11. Conclusion

If the dark photon is a mediator between the SM and dark sector, it can be searched for directly at the current or future e^+e^- colliders. If there is a splitting in the DM mass, the heavier DM decay can be recorded by a dedicated new small DM detector around the e^+e^- colliders. Such a DM detector can be placed in both forward and central directions, depending on whether the dark photon is on-shell. This new detector can search for parameter spaces not reached by previous experiments with the new BESIII and Belle II data, and can also re-open some parameter spaces that have been excluded by previous data derived with simple assumptions. Such a detector around BESIII can probe the dark photon coupling parameter ϵ down to $\sim 10^{-4}$, and if it is around Belle II, can further reach down to $\sim 10^{-5}$. For an off-shell dark photon, ϵ in the range between 10^{-3} and 10^{-2} can be excluded. It will open a new window for new physics searches related to a dark sector.

Acknowledgments

X. Chen and Z. Hu are supported by Tsinghua University Initiative Scientific Research Program. Y. Wu is supported by the Natural Sciences and Engineering Research Council of Canada (NSERC).

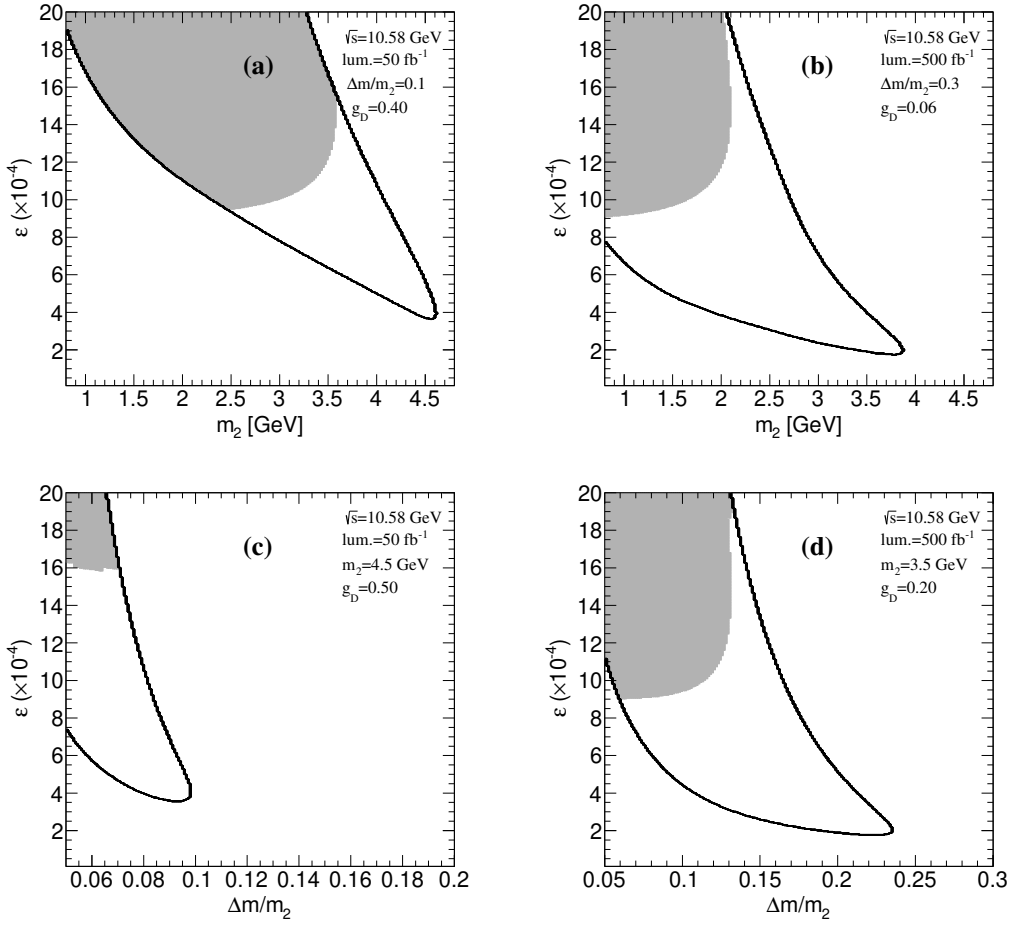

Figure 15: The 90% CL exclusion regions assuming zero background in ϵ vs. m_2 (a, b) and ϵ vs. $\Delta m/m_2$ (c, d) with two forward DM detectors placed on each side of Belle II, for the chosen model parameters (A' is on-shell) indicated in the plots. The gray areas in these plots have been excluded by BaBar. An optimal detector acceptance of 0.9% is assumed, as explained in the text.

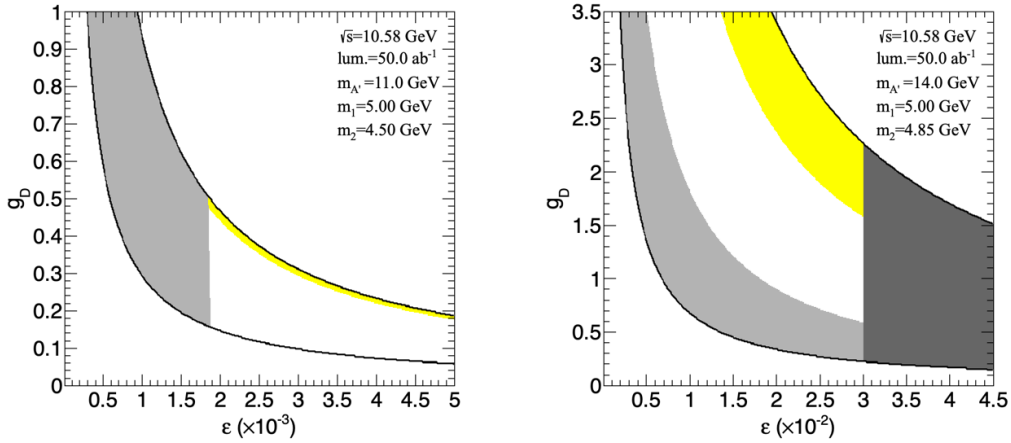

Figure 16: The 90% CL exclusion regions assuming zero background in ϵ vs. g_D with a single DM detector placed in the central direction near Belle II (Fig. 9(b)), for the chosen model parameters (A' is off-shell) indicated in the plots. The light gray areas are excluded by the relic density constraint, and the dark gray area is excluded by the LEP model-independent search [32]. The yellow area has an average ϕ_1 flight length $d < 1$ m.

References

[1] S. Andreas, C. Niebuhr and A. Ringwald, New limits on hidden photons from past electron beam dumps, Phys. Rev. D86 (2012) 095019. arXiv:1209.6083, doi:10.1103/PhysRevD.86.095019.

[2] J.P. Lees et al., BaBar Collaboration, Search for a dark photon in e^+e^- collisions at BABAR, Phys. Rev. Lett 113 (2014) 201801. arXiv:1406.2980, doi:10.1103/PhysRevLett.113.201801.

[3] J.P. Lees et al., BaBar Collaboration, Search for invisible decays of a dark photon produced in e^+e^- collisions at babar, Phys. Rev. Lett. 119 (2017) 131804. arXiv:1702.03327, doi:10.1103/PhysRevLett.119.131804.

[4] E. Aprile et al., XENON Collaboration, Dark Matter Search Results from a One Tonne×Year Exposure of XENON1T, Phys. Rev. Lett. 121 (2018) 111302. arXiv:1805.12562, doi:10.1103/PhysRevLett.121.111302.

[5] K. Schmidt-Hoberg et al., Constraints on light mediators: confronting dark matter searches with B physics, Physi. Lett. B727 (2013) 506. arXiv:1310.6752, doi:10.1016/j.physletb.2013.11.015.

[6] G. Krnjaic, Probing Light Thermal Dark-Matter With a Higgs Portal Mediator, Phys. Rev. D94 (2016) 073009. arXiv:1512.04119, doi:10.1103/PhysRevD.94.073009.

[7] J. Beacham et al., Physics Beyond Colliders at CERN: Beyond the Standard Model Working Group Report, J. Phys. G: Nucl. Part. Phys. 47 (2019) 1. arXiv:1901.09966, doi:10.1088/1361-6471/ab4cd2.

[8] A. Filimonova et al., Probing dark sectors with long-lived particles at BELLE II, Phys. Rev. D101 (2020) 095006. arXiv:1911.03490, doi:10.1103/PhysRevD.101.095006.

[9] N. Aghanim et al., Planck Collaboration, Planck 2018 results. VI. Cosmological parameters, A&A A6 (2020) 641. arXiv:1807.06209, doi:10.1051/0004-6361/201833910.

[10] D. Smith and N. Weiner, Inelastic Dark Matter, Phys. Rev. D64 (2001) 043502. arXiv:hep-ph/0101138, doi:10.1103/PhysRevD.64.043502.

[11] E. Izaguirre et al., Discovering Inelastic Thermal-Relic Dark Matter at Colliders, Phys. Rev. D93 (2016) 063523. arXiv:1508.03050, doi:10.1103/PhysRevD.93.063523.

[12] M. Duerr et al., Invisible and displaced dark matter signatures at Belle II, JHEP 02 (2020) 039. arXiv:1911.03176, doi:10.1007/JHEP02(2020)039.

[13] A. Berlin and F. Kling, Inelastic Dark Matter at the LHC Lifetime Frontier:ATLAS, CMS, LHCb, CODEX-b, FASER, and MATHUSLA, Phys. Rev. D99 (2019) 015021. arXiv:1810.01879, doi:10.1103/PhysRevD.99.015021.

[14] E. Izaguirre, Y. Kahn, G. Krnjaic and M. Moschella, Testing Light Dark Matter Coannihilation With Fixed-Target Experiments, Phys. Rev. D96 (2017) 055007. arXiv:1703.06881, doi:10.1103/PhysRevD.96.055007.

[15] G. Belanger et al., micrOMEGAs5.0 : freeze-in, Comput. Phys. Commun. 231 (2018) 173. arXiv:1801.03509, doi:10.1016/j.cpc.2018.04.027.

[16] J. Jiang, H. Yang and C.-F. Qiao, Exploring Bosonic Mediator of Interaction at BESIII, Euro. Phys. Jour. C79 (2019) 404. arXiv:1810.05790, doi:10.1140/epjc/s10052-019-6912-3.

[17] M. Tanabashi et al., Particle Data Group, Review of Particle Physics, Phys. Rev. D98 (2018) 030001. doi:10.1103/PhysRevD.98.030001. URL http://pdg.lbl.gov/2019/hadronic-xsections/hadron.html

[18] M. Komatsu, OPERA experiment, Nucl. Instrum. Meth. A503 (2003) 124. doi:10.1016/S0168-9002(03)00653-3. URL http://cds.cern.ch/record/642973

[19] S. Aoki et al., DsTau Collaboration, DsTau: study of tau neutrino production with 400 GeV protons from the CERN-SPS, JHEP 01 (2020) 033. arXiv:1906.03487, doi:10.1007/JHEP01(2020)033.

[20] H. Abreu et al., FASER Collaboration, Detecting and Studying High-Energy Collider Neutrinos with FASER at the LHC, Euro. Phys. Jour. C80 (2020) 61. arXiv:1908.02310, doi:10.1140/epjc/s10052-020-7631-5.

[21] S. Agostinelli et al., Geant4 — a simulation toolkit, Nucl. Instrum. Meth. A506 (2003) 250. doi:10.1016/S0168-9002(03)01368-8. URL http://cds.cern.ch/record/602040

[22] L. Shekhtman et al., Development of μ-RWELL detectors for the upgrade of the tracking system of CMD-3 detector, Nucl. Instrum. Meth. A936 (2019) 401. doi:10.1016/j.nima.2018.11.033.

[23] M. Ablikim et al., Design and Construction of the BESIII Detector, Nucl. Instrum. Meth. A614 (2010) 345. arXiv:0911.4960, doi:10.1016/j.nima.2009.12.050.

[24] K. Altenmuller et al., KATRIN Collaboration, Muon-induced background in the KATRIN main spectrometer, Astropart. Phys. 108 (2019) 40. arXiv:1805.12173, doi:10.1016/j.astropartphys.2019.01.003.

[25] P. Shukla and S. Sankrith, Energy and angular distributions of atmospheric muons at the EartharXiv:1606.06907.

[26] T. Fukuda et al., The analysis of interface emulsion detector for the OPERA experiment in JAPAN Scanning facility, J. of Instrum. 5 (2010) 04009. doi:10.1088/1748-0221/5/04/P04009.

[27] D. J. Lange, The EvtGen particle decay simulation package, Nucl. Instrum. Meth. A462 (2001) 152. doi:10.1016/S0168-9002(01)00089-4.

[28] S. Jadach, B.F.L. Ward and Z. Was, The precision Monte Carlo event generator KK for two-fermion final states in e^+e^- collisions, Comput. Phys. Commun. 130 (2000) 260. arXiv:hep-ph/9912214, doi:10.1016/S0010-4655(00)00048-5.

[29] S. Jadach, B.F.L. Ward and Z. Was, Coherent exclusive exponentiation for precision Monte Carlo calculations, Phys. Rev. D63 (2001) 113009. arXiv:hep-ph/0006359, doi:10.1103/PhysRevD.63.113009.

[30] E. Kou et al., Belle II Collaboration, The Belle II Physics Book, Prog. Theor. Exp. Phys. 12 (2019) 123C01. arXiv:1808.10567, doi:10.1093/ptep/ptz106.

[31] K. Jodłowski, F. Kling, L. Roszkowski and S. Trojanowski, Extending the reach of FASER, MATHUSLA, and SHiP towards smaller lifetimes using secondary particle production, Phys. Rev. D101 (2020) 095020. arXiv:1911.11346, doi:10.1103/PhysRevD.101.095020.

[32] A. Hook, E. Izaguirre and J. G. Wacker, Model Independent Bounds on Kinetic Mixing, Adv. High Energy Phys. 2011 (2011) 859762. arXiv:1006.0973, doi:10.1155/2011/859762.